RESEARCH ARTICLE
doi: 10.2306/scienceasia1513-1874.2026.018

ScienceAsia 52 (1): 2026: ID 2026018: **1–10**

Preparation of Fe_3O_4@SiO_2@NH_2-FLX magnetic nanomaterials and investigation of their ability to capture Gram-negative and Gram-positive bacteria

Yang Jinchuan[a], **Peng Yuanyuan**[a], **Fu Hua**[a,*], **Tao Lixia**[b]

[a] College of Chemical Engineering, Qinghai University, Xining 810016 China
[b] Zhejiang Boshi Hua Environmental Protection Technology Co., Ltd. (Group), Zhejiang 310015 China

*Corresponding author, e-mail: 1171299733@qq.com

Received 11 Sep 2025, Accepted 4 Feb 2026
Available online 21 Feb 2026

ABSTRACT: Magnetic nanomaterials are widely used in microbial enrichment due to their magnetic response and biocompatibility. However, in high-salinity environments, they tend to agglomerate, impairing dispersion. To improve microbial adsorption in such conditions, this study used a solvothermal method to synthesize Fe_3O_4 nanoparticles coated with SiO_2 and modified with amino (—NH_2) and fleroxacin (-FLX) groups, creating Fe_3O_4@SiO_2@NH_2-FLX. The ability of the nanomaterial to capture *Staphylococcus aureus* and *Escherichia coli*, its adsorption behavior, kinetics, and thermodynamics were evaluated. Confirmed by SEM, XRD, XPS, FT-IR, and VSM, the nanomaterial showed maximum adsorption for *E. coli* and *S. aureus* at 4 and 15 min, with efficiencies of 97% and 95%, respectively. Under optimal conditions, it outperformed unmodified and mono-aminated nanomaterials, achieving over 95% capture in Qarhan Salt Lake brine. Cyclic tests showed 80% efficiency after five cycles. In real saline samples, it retained about 90% efficiency for halophilic bacteria. Overall, this dual-functionalized nanoparticle offers significant advantages for removing bacteria from aquatic environments.

KEYWORDS: magnetic nanoparticles, bifunctional materials, *S. aureus*, *E. coli*, bacterial capture

INTRODUCTION

Microorganisms are the oldest, most abundant, and most diverse life forms on Earth [1]. They are not only the engines of Earth's ecosystems and a stable foundation but also important productive forces driving the development of human medicine, food, agriculture, and industry [2–4]. For instance, in the high-salt, pH-neutral lakes of the Kurendah grassland [5] (Russia), aerobic bacteria capable of degrading chitin (*Arhodomonas* and *Arhodomonas spp.*) have been enriched. A study of the coastal salt pans of South Africa [6] found that, based on amplification of dissimilatory sulfite reductase genes, Desulfobacteraceae (complete oxidizers) and Halodesulfobacteriaceae (incomplete oxidizers) remain active at salinities as high as 300–400%. In the medical field, certain bacterial-induced diseases [7] (such as sepsis) require the enrichment, detection, and identification of bacteria. Today, the application of microorganisms has permeated all aspects of human production and life, and the control of microorganisms in high-salt brine environments is a common challenge faced by multiple industrial fields. Such environments [8] typically feature high ionic strength, high osmotic pressure, and strong corrosiveness. Traditional sterilization methods such as chemical disinfectants are limited in high-salt environments and may produce toxic by-products, causing secondary pollution. We hope to capture bacteria in a more efficient and environmentally friendly way. The novel and efficient bacterial capture technology—magnetic nanomaterials [9, 10]—has become a research hotspot due to their unique physical and chemical properties. As a new type of functional material, magnetic nanomaterials have shown great potential in the field of bacterial capture. These materials usually have a core-shell structure, with iron oxide as the core, providing superparamagnetic properties. Through surface functionalization [11, 12], such as high-molecular polymers, antibiotic drugs, or specific ligands, magnetic nanomaterials can selectively bind to target bacteria. Under the action of an external magnetic field, the complexes of the material and bacteria can be rapidly separated and enriched, achieving efficient capture and simple recovery of microorganisms [13]. This technology avoids the cumbersome operations of traditional methods such as centrifugation and filtration and is particularly suitable for high-salt and other difficult environments.

Currently, several studies have explored the method of combining antibiotics with magnetic nanomaterials for the enrichment and detection of microorganisms such as bacteria. Yang et al [14] functionalized magnetic nanoparticles by introducing amino groups and subsequently conjugated polyethylene glycol (PEG) to these groups, followed by the attachment of vancomycin (Van) as the terminal ligand. The resulting multivalent brush magnetic nanoprobe (Van-PEG-PL-MNP) demonstrated a high enrichment efficiency (>94%) for Listeria monocytogenes. Rashid et al [15] reported that vancomycin-conjugated magnetic nanoparticles exhibited effective

antibacterial activity and strong binding affinity toward both Gram-positive and Gram-negative bacteria. Abdurhaman et al [16] synthesized Al/Van-PDA-MNPs by conjugating allantoin (Al) and vancomycin onto dopamine-coated magnetic nanoparticles. This approach enabled rapid bacterial enrichment in blood samples, reducing the PCR detection limit to 10^{-2} CFU/ml. Li et al [17] developed Kan@MNPs and Ery@MNPs by modifying magnetic nanoparticles with kanamycin (Kan) and erythromycin (Ery), respectively. These nanoparticles were further combined with lysozyme to facilitate the rapid extraction of pathogenic bacterial DNA from blood samples.

Fleroxacin (FLX), a trifluoroquinolone antibacterial agent, possesses a broad antibacterial spectrum and exhibits potent antibacterial activity [18, 19]. It demonstrates effective antimicrobial action against both Gram-negative and Gram-positive bacteria, particularly under aerobic and facultative anaerobic conditions. By conjugating fleroxacin as a functional group onto the surface of magnetic nanoparticles, it may be possible to achieve efficient bacterial capture.

In this study, Fe_3O_4 nanoparticles were synthesized using the solvothermal method. Subsequently, the surface of the Fe_3O_4 particles was coated with SiO_2, and amino groups were introduced onto the surface of the Fe_3O_4@SiO_2 carriers through a coupling reaction between surface silanol (Si—OH) groups and ethoxy groups of 3-aminopropyltriethoxysilane. To enhance the density of surface amino groups and improve the bacterial adsorption capacity of the material, aldehyde groups (—CHO) were introduced onto the magnetic spheres via a nucleophilic addition reaction between primary amine groups and glutaraldehyde. These aldehyde groups were then used to further graft polyethylenimine, which is rich in primary amine groups, onto the surface of the Fe_3O_4@SiO_2 carrier. Finally, FLX was immobilized onto the material surface through an amidation reaction between the carboxyl group of FLX and part of the primary amine groups on polyethylenimine, resulting in the construction of a magnetic nano-solid-phase extractant, Fe_3O_4@SiO_2@NH_2-FLX, co-modified with amino groups. The synthesis route of the material is illustrated in Fig. 1, and the bacterial adsorption process is depicted in Fig. 2.

MATERIALS AND METHODS

Reagents and instruments

Scanning electron microscopy (SEM, Carl Zeiss AG, Oberkochen, Germany) was employed to investigate the morphological structure of the materials. Fourier transform infrared (FT-IR, Thermo Fisher Scientific Inc., Massachusetts, USA) spectroscopy was utilized to analyze functional groups within the materials. X-ray diffraction (XRD, Rigaku Corporation, Tokyo, Japan) was applied to study the crystalline structure of the materials within the range of 5° to 90°. A High-Speed Fully Automatic Multifunctional High-Performance X-ray Photoelectron Spectrometer (XPS, Thermo Fisher Scientific Inc.) was employed to analyze the chemical elements before and after material modification. A Vibrating Sample Magnetometer (VSM, Quantum Design, California, USA) was used to analyze the magnetic saturation strength of the samples.

All reagents used in the material synthesis during the experiment were supplied by Aladdin Biochemical Technology Co., Ltd. (China) The experimental strains, including *E. coli*, *S. aureus*, and halophilic bacteria, were all cultured and provided by the same research laboratory. The brine utilized in the experiment was obtained from the Chaka Salt Lake and was at saturated concentration.

Material preparation

Preparation of Fe_3O_4, Fe_3O_4@SiO_2, and Fe_3O_4@SiO_2@PEI:

The Fe_3O_4 magnetic nanoparticles were synthesized via a solvothermal method as described [20]. The Fe_3O_4@SiO_2 composite was then prepared according to the published methods [21, 22]. In this process, the Fe_3O_4 nanoparticles were coated with silica via the hydrolysis and polycondensation of tetraethyl orthosilicate (TEOS), forming an amorphous silica layer.

Amino modification and crosslinking of polyethyleneimine (PEI) materials involve a two-step process. First, 3-aminopropyltriethoxysilane (APTES) is used to introduce amino groups onto the surface of Fe_3O_4@SiO_2 particles. Subsequently, glutaraldehyde (GA) serves as a crosslinking agent, with its dialdehyde groups reacting with amino groups on both Fe_3O_4@SiO_2 and PEI molecules. This reaction forms Schiff base linkages (—C=N—), which are then reduced (e.g., with $NaBH_4$) and stabilized as secondary amine bonds (—C—N—), thereby crosslinking PEI. Detailed experimental procedures are as described [23, 24].

Preparation of Fe_3O_4@SiO_2@NH_2-FLX:

One hundred milliliters of dimethyl sulfoxide (DMSO) was measured into a 250 ml three-necked flask and ultrasonically degassed for 10 min. Then, 1.0 g of Fe_3O_4@SiO_2@PEI particles was addded to the flask. The reaction apparatus was sealed, and the system was purged with nitrogen to remove residual oxygen. A total of 0.104 g of FLX and 0.2 g of 1-ethyl-3-(3-dimethylaminopropyl)carbodiimide hydrochloride (EDC) were weighed, dissolved in a small volume of DMSO, and slowly injected into the three-necked flask using a syringe. The system was purged again with nitrogen, the reaction mixture was heated to 55 °C, and this temperature was maintained for 24 h. The resulting product, Fe_3O_4@SiO_2@NH_2-FLX, is then washed repeatedly with deionized water and ethanol, followed by vacuum drying at 40 °C.

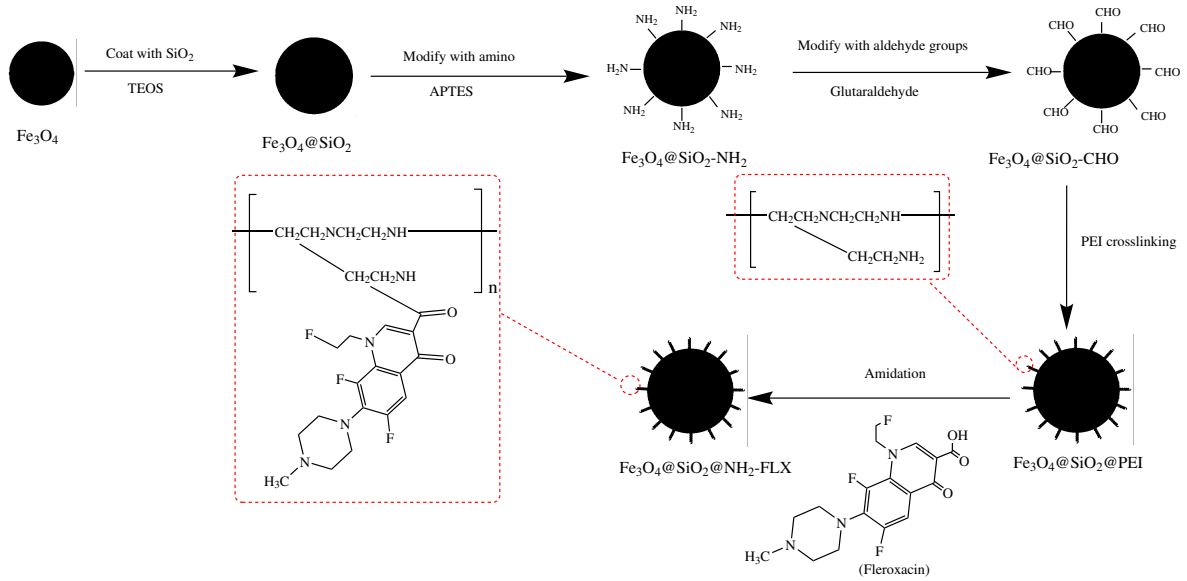

Fig. 1 Preparation schematic for Fe_3O_4@SiO_2@NH_2-FLX nanomaterials.

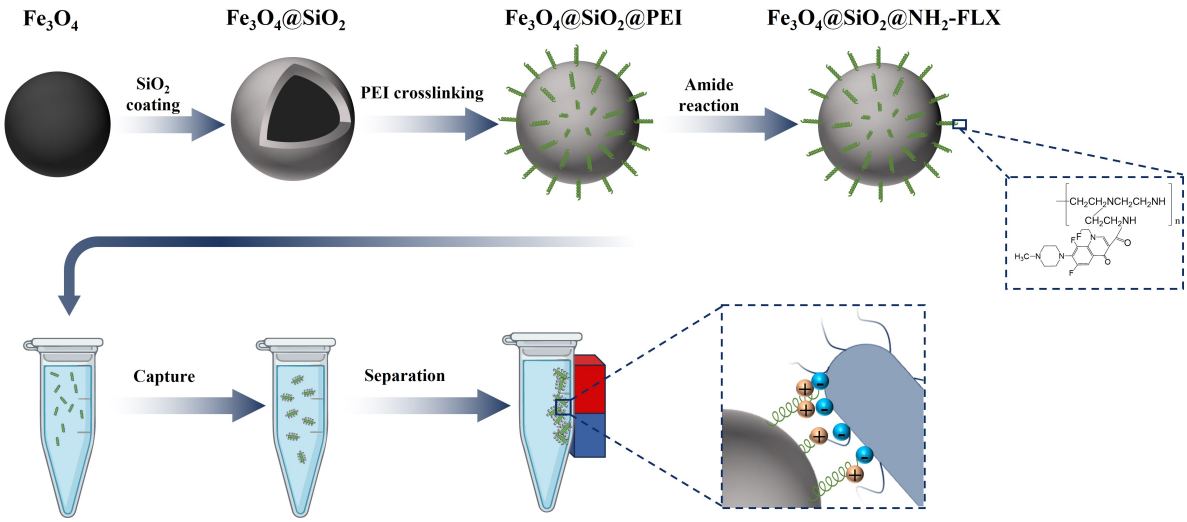

Fig. 2 Preparation of Fe_3O_4@SiO_2@NH_2-FLX nanomaterials and schematic diagram of bacterial adsorption process.

Adsorption experiments

The adsorption experiment employed two representative and commonly studied bacterial species: Gram-positive (*S. aureus*) and Gram-negative (*E. coli*). The bacterial cultures were stored at 4 °C and required prior incubation before use. The detailed procedural steps are as follows: the refrigerated bacterial suspension was placed in an air bath shaker, where the temperature was maintained at 37 °C and the agitation speed at 150 rpm. After a 16 h incubation, the culture was transferred to a centrifuge and spun at 5000 rpm for 5 min. The pellet was washed and resuspended three times with phosphate-buffered saline (PBS, pH = 7.2) and then diluted with the same buffer. An appropriate volume of the resulting suspension was taken, and its optical density (OD) at 600 nm was measured. The concentration of the bacterial suspension was adjusted to achieve the desired OD_{600} value (ranging from 0.1 to 1), serving as the final bacterial sample for either *E. coli* or *S. aureus*. The initial absorbance value (A_0) of the sample was recorded.

Five milligrams of Fe_3O_4@SiO_2@NH_2-FLX material was accurately weighed and briefly ultrasonicated to ensure complete dispersion of the synthesized magnetic nanomaterials. Subsequently, 2 ml of the *E. coli* sample was added to each reaction system. The adsorption efficiency was investigated at varying sample

dosages. The pH of the buffer solution was adjusted, and bacterial suspensions were prepared at pH values of 3, 5, 6, 7, 8, 9, and 11 to determine the optimal pH for adsorption efficiency. The standard curves for *E. coli* and *S. aureus* were constructed based on previously reported methods [25]. The OD_{600} values of the supernatants collected at different time intervals were measured using an enzyme-linked immunosorbent assay (ELISA) reader to evaluate the adsorption kinetics of the magnetic nanoparticles toward *E. coli* and *S. aureus*.

The adsorption efficiency is calculated using the following formula:

$$E = \frac{A_0 - A}{A_0} \times 100\%$$

where E denotes the adsorption efficiency, A_0 represents the absorbance of the bacterial suspension before adsorption, and A refers to the absorbance after adsorption.

The study further compared the adsorption efficiencies of various materials. The adsorption behaviors of Fe_3O_4, Fe_3O_4@SiO_2, and Fe_3O_4@SiO_2@PEI toward *E. coli* and *S. aureus* were consistent with previously observed trends. In addition, brine from Chaka Salt Lake was used as an alternative to PBS buffer to evaluate the adsorption capacity of the materials under brine conditions and to assess their cyclic adsorption performance. The cyclic adsorption procedure was as follows: after magnetic materials were introduced for adsorption, the supernatant was removed using a magnet, leaving the magnetic material-bacteria complex. A suitable volume of sterile water with a pH of 2–3 was then added, followed by magnetic separation to remove the supernatant. This process was repeated 2–3 times. Subsequently, PBS buffer at pH 6 was added to neutralize the material and restore its adsorption capability. The cyclic adsorption process was then repeated for subsequent rounds.

RESULTS AND DISCUSSION

Microstructure and phase constituent

Microscopic morphology

Fig. 3(a–c) presents scanning electron microscope (SEM) images of the prepared materials Fe_3O_4, Fe_3O_4@SiO_2@PEI, and Fe_3O_4@SiO_2@NH_2-FLX, observed at magnifications of 10,000× and 100,000×, respectively. As shown in Fig. 3(a), Fe_3O_4 exhibits uniformly sized spherical particles with diameters ranging from 200 to 250 nm under the same magnification. In Fig. 3(b), the particle size of Fe_3O_4@SiO_2@PEI is significantly increased to approximately 400 nm, and the transparent surface coating suggests that the Fe_3O_4 core has been fully encapsulated by SiO_2 and polyethyleneimine layers. The SEM image of Fe_3O_4@SiO_2@NH_2-FLX reveals a particle size of approximately 400–450 nm. Compared with Fe_3O_4@SiO_2@PEI, the particle size remains relatively unchanged; however, irregular flap-like protrusions are observed on the surface, indicating that further chemical reactions have occurred on the material surface.

The XRD characterization results of Fe_3O_4, Fe_3O_4@SiO_2, Fe_3O_4@SiO_2@PEI, and Fe_3O_4@SiO_2@NH_2-FLX are presented in Fig. 4(a). As shown in Fig. 4(a), the 2θ diffraction angle range of Fe_3O_4 spans from 20° to 80°, with distinct diffraction peaks observed at 18.3°, 30.1°, 35.5°, 37.1°, 43.1°, 53.5°, 57.0°, 62.6°, and 74.0°, corresponding to the crystal planes (111), (220), (311), (222), (400), (422), (511), (440), and (533), respectively [26]. These well-defined peaks suggest a high degree of crystallinity. In contrast, broad "hump-like" peaks observed between 15° and 30° (2θ) for Fe_3O_4@SiO_2, Fe_3O_4@SiO_2@NH_2, and Fe_3O_4@SiO_2@NH_2-FLX are characteristic of amorphous silica [27], confirming the successful coating of silica on the Fe_3O_4 surface. Additionally, the reduced peak intensities observed for Fe_3O_4@SiO_2@PEI and Fe_3O_4@SiO_2@NH_2-FLX suggest further crosslinking of polyethyleneimine. Throughout the modification process, the peak positions and relative intensities remained consistent with the standard diffraction data for Fe_3O_4 (JCPDS No. 65-3107), indicating that the crystal structure of Fe_3O_4 was preserved during the synthesis of the bifunctional magnetic nanoparticles.

Material composition

Fig. 4(b) presents the infrared spectra of fleroxacin, Fe_3O_4@SiO_2@NH_2-FLX, and Fe_3O_4@SiO_2, from top to bottom. Comparison of the three spectra shows that the fleroxacin-functionalized Fe_3O_4 magnetic nanomaterial exhibits characteristic absorption peaks at 1718 and 1630 cm^{-1}, corresponding to the carbonyl and amide groups, respectively, in fleroxacin propionate. This indicates that FLX has been successfully grafted onto the surface of the magnetic spheres following a two-step amino functionalization process. Fig. 5 displays the full XPS spectra of Fe_3O_4 and Fe_3O_4@SiO_2@NH_2-FLX. In the full scan spectrum of Fig. 5(a), the Fe 2p peak intensity of Fe_3O_4@SiO_2@NH_2-FLX is significantly reduced, consistent with the diminished Fe_3O_4 diffraction peak intensity observed in XRD after modification and encapsulation. Meanwhile, the characteristic signal peaks of F 1s, N 1s, Si 2s, and Si 2p are clearly visible. Fig. 5(b) presents the Fe 2p fine spectrum of Fe_3O_4. The peak at 723.6 eV corresponds to Fe 2p1/2, while the peak regions at 710.4 and 713.6 eV correspond to Fe 2p3/2, indicating [28] the coexistence of Fe^{2+} and Fe^{3+} in Fe_3O_4. The satellite peaks [29] at 716.9, 729.9, and 732.3 eV correspond to Fe 2p. Fig. 5(c) and (d) show the changes in C 1s and O 1s peaks

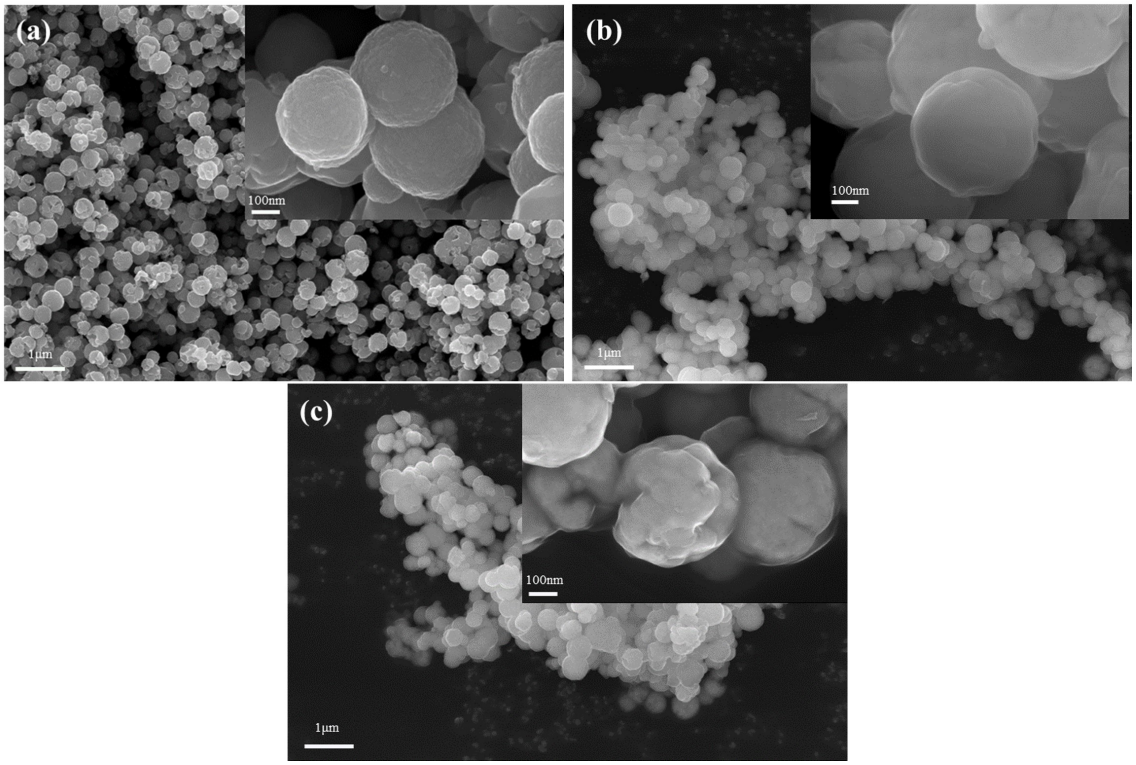

Fig. 3 SEM images of (a) Fe_3O_4, (b) Fe_3O_4@SiO_2@NH_2, and (c) Fe_3O_4@SiO_2@NH_2-FLX.

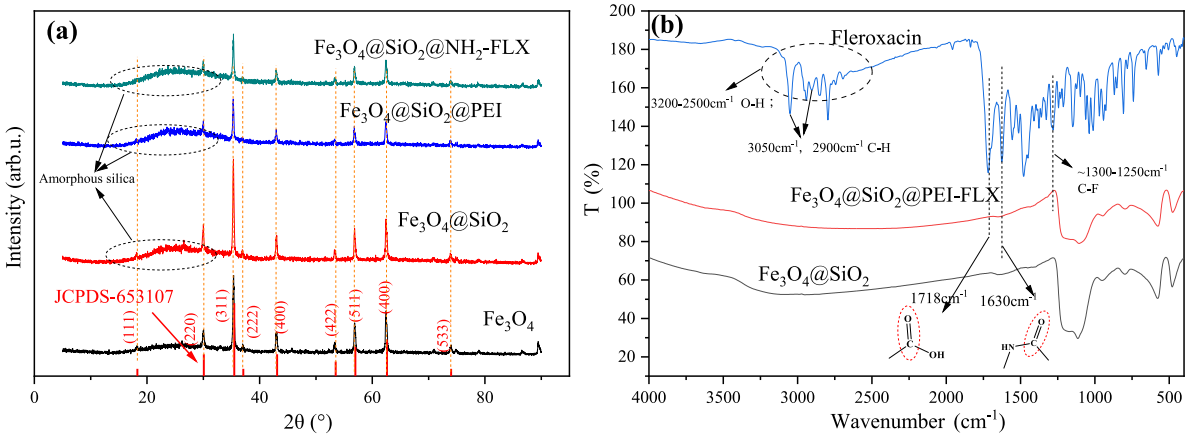

Fig. 4 (a) XRD patterns of Fe_3O_4, Fe_3O_4@SiO_2, Fe_3O_4@SiO_2@PEI, and Fe_3O_4@SiO_2@NH_2-FLX and (b) FT-IR spectra of Fe_3O_4@SiO_2, Fleroxacin, and Fe_3O_4@SiO_2@NH_2-FLX.

before and after modification, calibrated against the C—C peak at 284.8 eV. The C—O functional group [30] binding energy at 286.5 eV decreased to 286.3 eV, while the peak area of metallic lattice oxygen (O^{2-}) at 529.9 eV diminished due to the formation of Si—O bonds (533.0 eV). This indicates that the Fe_3O_4 coating on SiO_2 enhances the electron density around carbon atoms. The C=O functional group binding energy increased from 288.4 eV to 288.7 eV, likely due to C atoms bonding with more electronegative groups (N, F), raising the C atom binding energy. Fig. 5(e) shows two N peaks: the peak at 399.5 eV corresponds to imino or amide groups, revealing the formation of amide bonds during modification; the protonated amine at 401.6 eV arises from the protonation of amino groups, simultaneously explaining the positive charge on the material surface. This indicates successful surface modification with amino and fluoroquinolone groups. Elemental composition before and after modification is summarized in Table S1.

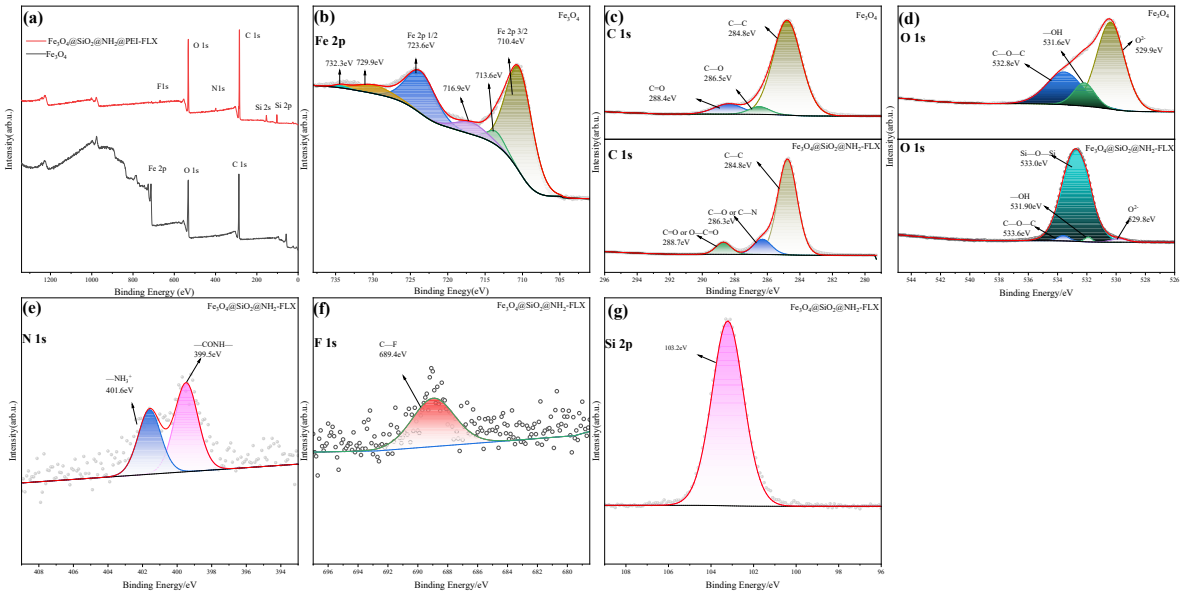

Fig. 5 XPS profiles of Fe_3O_4 and Fe_3O_4@SiO_2@NH_2-FLX; (a) Survey spectrum, (b) Fe 2p, (c) C 1s, (d) O 1s (e)N 1s, (f) F 1s, and (g) Si 2p.

It can be observed from the hysteresis loop shown in Fig. S1(a) that the magnetic nanoparticles retain strong superparamagnetic properties after surface coating and functional group modification. The saturation magnetization values are 87.5 emu/g for Fe_3O_4, 67.2 emu/g for Fe_3O_4@SiO_2@PEI, and 68.1 emu/g for Fe_3O_4@SiO_2@NH_2-FLX. The reduction in saturation magnetization is primarily attributed to the complete coverage of the SiO_2 layer on the particle surface, whereas the crosslinking of PEI has minimal influence on the material's magnetic properties. Fig. S1(b) presents the Fe_3O_4@SiO_2@NH_2-FLX magnetic nanomaterial dispersed in an ethanol solution prepared in this study. As shown in the left image, after ultrasonic treatment, the material is uniformly dispersed in the solution and remains stable without precipitation for at least 30 min in the absence of an external magnetic field. Upon application of an external magnetic field, the Fe_3O_4@SiO_2@NH_2-FLX nanoparticles are rapidly attracted to the magnet, demonstrating strong magnetic responsiveness. These observations indicate that this magnetic adsorbent can be efficiently separated from the sample matrix under an external magnetic field, enabling rapid and effective recovery.

Optimal adsorption and comparison of different adsorption materials

Standard curves for E. coli and S. aureus

Fig. S2(a) and (b) show the standard curves for *E. coli* and *S. aureus*, respectively. The linear expression of the *E. coli* standard curve is $\log(\text{concentration}) = 8.339 + 1.264\log(\text{OD}_{600})$, $R^2 = 0.991$.

The expression of the *S. aureus* standard curve is $\log(\text{concentration}) = 7.906 + 1.154\log(\text{OD}_{600})$, $R^2 = 0.997$.

In the expression, concentration refers to the bacterial concentration, with units of CFU/ml; OD_{600} refers to the corresponding optical density value at each concentration.

The effect of pH on the zeta potential of materials and the capture efficiency of Fe_3O_4@SiO_2@NH_2-FLX materials on E. coli and S. aureus at different pH levels

To evaluate the adsorption capacity of the material toward two bacterial species under optimal conditions, the adsorption efficiency of Fe_3O_4@SiO_2@NH_2-FLX was measured across a pH range of 3 to 11. As illustrated in Fig. S3(a), the maximum adsorption efficiency for both bacterial strains was observed at pH 6. The isoelectric point (pH) [31] of *E. coli* typically falls within the range of 4 to 5, whereas that of *S. aureus* lies between 3 and 4. A decrease in environmental pH weakens electrostatic interactions, thereby reducing adsorption efficiency. Similarly, excessively alkaline conditions may impair bacterial viability, which in turn lowers the adsorption capacity. As shown in Fig. S3(b), zeta potential measurements of the material at varying pH levels indicate that Fe_3O_4 exhibits a positive surface charge below pH 8.5 and a negative charge above this value. Following amino functionalization, the material's surface charge becomes predominantly positive. Therefore, both the dispersion behavior and surface charge characteristics of the material at different pH levels play a significant role in influencing bacterial adsorption efficiency.

Different amounts of additives having different effects on trapping

The synthesis of Fe_3O_4@SiO_2@NH_2-FLX at varying FLX loadings was conducted to investigate how FLX content affects bacterial capture efficiency (Fig. S4). Experimental results indicate that when the mass ratio of m(Fe_3O_4@SiO_2@PEI) to m(FLX) is 10:3, the material demonstrates effective capture of *E. coli*. In contrast, when the ratio is 10:1, a higher capture efficiency is observed for *S. aureus*. These findings suggest that different FLX loadings yield distinct adsorption behaviors for the two bacterial strains. FLX, a fluoroquinolone antibiotic, primarily exerts its antibacterial effect by inhibiting bacterial DNA gyrase (topoisomerase II) and topoisomerase IV. When FLX is immobilized on the surface of nanomaterials, it may influence bacterial adsorption through several mechanisms: (1) Specific binding: FLX can interact with target proteins on the bacterial cell membrane such as DNA gyrase, thereby enhancing the bacterial capture capability of the material. (2) Charge effects: at physiological pH, FLX molecules may carry a negative charge or exist in a zwitterionic state, which can alter the overall surface charge of the material [32], thereby influencing electrostatic interactions and adsorption behavior. Therefore, the concentration of FLX introduced during material preparation significantly affects adsorption performance for different bacterial species. Based on these results, subsequent experiments were carried out using materials exhibiting optimal bacterial adsorption efficiency.

Bacterial capture efficiency of different materials

As illustrated in Fig. S5, the bifunctional nanomaterial Fe_3O_4@SiO_2@NH_2-FLX exhibits significantly higher adsorption efficiency for *E. coli* and *S. aureus* than other nanomaterials, including those without amino group modification and those with only amino group modification (Fe_3O_4, Fe_3O_4@SiO_2, and Fe_3O_4@SiO_2@PEI). Iron-based nanoparticles without an SiO_2 coating exhibit inferior dispersion and biocompatibility compared with their coated counterparts. However, after cross-linking with polyethyleneimine, the surface of the nanomaterial becomes enriched with positively charged amino functional groups, and electrostatic adsorption becomes the dominant mechanism [23]. This characteristic significantly enhances the enrichment efficiency for negatively charged bacteria. Additionally, the fleroxacin-modified material contains fluorine and oxygen elements in its molecular structure, which contribute to strong oxidative properties that effectively inhibit bacterial DNA gyrase activity, thereby achieving a bactericidal effect [19]. Consequently, the antibacterial properties of fleroxacin are harnessed to further improve both the efficiency and speed of bacterial capture.

The molecular-level interactions between fluoroquinolone functional groups grafted onto adsorbent surfaces and bacterial membranes primarily involve three aspects: transmembrane penetration [33], efflux pump recognition [34], and biofilm penetration [35]: 1. At physiological pH, fluoroquinolones primarily exist as zwitterionic forms. They traverse the outer membrane by electrostatic binding to charged residues lining the bacterial OmpF channel, thereby inhibiting efflux. 2. Drug molecules are recognized and captured by the distal binding site of the bacterial AcrB transporter, enhancing efflux efficiency. 3. Drug penetration is enhanced by disrupting or inhibiting biofilm matrix synthesis (i.e., extracellular polysaccharide complexes). Studies indicate that disrupting the biofilm promotes drug entry into bacteria. In summary, FLX exhibits electrostatic interactions with the OmpF channel protein on the bacterial membrane during penetration. Furthermore, the AcrB transporter on the bacterial membrane recognizes and captures FLX during active efflux. Consequently, the modified nanomaterial Fe_3O_4@SiO_2@NH_2-FLX demonstrates exceptional bacterial capture efficacy.

Isothermal adsorption and adsorption kinetics

The amount of bacteria adsorbed onto the material Fe_3O_4@SiO_2@NH_2-FLX is expressed as follows:

$$Q_e = \frac{(C_0 - C_e) \times V}{m} \tag{1}$$

Langmuir isothermal adsorption linear expression:

$$\frac{C_e}{Q_e} = \frac{C_e}{Q_m} + \frac{1}{Q_m K_L} \tag{2}$$

Freundlich isothermal adsorption linear expression:

$$\ln Q_e = \ln K_F + \frac{1}{n} \ln C_e \tag{3}$$

In the aforementioned formulas, Q_e denotes the equilibrium amount of bacteria adsorbed per unit mass of the adsorbent, expressed in CFU/g. C_0 refers to the initial bacterial concentration, while C_e represents the bacterial concentration at equilibrium, measured in CFU/ml. V indicates the volume of the solution in ml, and m denotes the mass of the adsorbent in g. Q_m signifies the theoretical maximum adsorption capacity of the adsorbent per unit mass, also expressed in CFU/g. K_L is the Langmuir constant, with units of ml/CFU, and K_F is the Freundlich adsorption capacity constant, reflecting the adsorption strength, with units of $[(\text{CFU/g})\cdot(\text{ml/CFU})^{1/n}]$. The parameter n represents the adsorption intensity constant, indicating the degree of difficulty of the adsorption process, and is dimensionless.

Based on the fitting results of the Langmuir and Freundlich isotherm adsorption models (Fig. S6(a–d)) and the parameters presented in Table S2, it can be

concluded that the Langmuir model provides a better fit for *E. coli*. This indicates that the adsorption process for *E. coli* is predominantly monolayer in nature, with relatively uniform adsorption sites on the surface of the adsorbent [36–38]. For *S. aureus*, the Langmuir model also demonstrates a reasonable fit, although not as strong as for *E. coli*, whereas the Freundlich model shows poor correlation. This suggests that the adsorption behavior of *S. aureus* is primarily consistent with monolayer adsorption, although with a certain degree of heterogeneity in the adsorption sites.

To investigate the adsorption rate of bacteria on material surfaces and study the adsorption mechanism, kinetic simulations of the adsorption processes of *E. coli* and *S. aureus* were conducted using simple kinetic models, including first-order and second-order models, whose expressions are as follows:

$$Q_t = \frac{(C_0 - C_t) \times V}{m} \tag{4}$$

Pseudo-first-order kinetic equation expression:

$$Q_t = Q_e(1 - e^{-K_1 t}) \tag{5}$$

Pseudo-second-order kinetic equation expression:

$$\frac{t}{Q_t} = \frac{1}{K_2 Q_e^2} + \frac{t}{Q_e} \tag{6}$$

Fig. S6(e–h), in conjunction with the kinetic parameters presented in Table S3, indicate that both physical and chemical adsorption may occur simultaneously during the adsorption process involving *E. coli*. However, the better fit of the pseudo-second-order kinetic model suggests that chemical adsorption is likely the dominant mechanism, although physical adsorption also plays a minor role. In the case of *S. aureus*, the first-order kinetic model is not applicable, whereas the pseudo-second-order model demonstrates an excellent fit. This implies that the adsorption mechanism is predominantly chemical in nature [31, 39]. The strong chemical interactions between the adsorbate (*S. aureus*) and the adsorbent may involve chemical processes such as ion exchange, covalent bond formation, or coordination bond formation [40].

Adsorption thermodynamics and related parameters

Two types of bacteria were adsorbed within a temperature range of 25 °C to 45 °C, and the thermodynamic parameters of the adsorption process were systematically investigated. As illustrated in Fig. S7(c), the equilibrium adsorption capacity of Fe_3O_4@SiO_2@NH_2-FLX for both bacterial species gradually decreases with increasing temperature, indicating that the adsorption process is exothermic.

The thermodynamic parameters, including the enthalpy change ΔH^0 (kJ/mol), entropy change ΔS^0 [J/(mol·K)], and Gibbs free energy change ΔG^0 (kJ/mol), were calculated using the following equations:

$$\ln K_T = \frac{\Delta S^0}{R} - \frac{\Delta H^0}{RT} \tag{7}$$

$$\Delta G^0 = -RT \ln K_T \tag{8}$$

$$K_T = \frac{Q_e}{C_e} \tag{9}$$

In equations (7) to (9), Q_e and C_e denote the equilibrium adsorption capacity and the equilibrium concentration at the respective temperatures. K_T (l/g), R (8.314 kJ/mol), and T (K) represent the equilibrium constant, the universal gas constant, and the absolute temperature, respectively.

As shown in Fig. S7 and Table S4, the adsorption of *E. coli* and *S. aureus* is both spontaneous and exothermic. An increase in temperature reduces adsorption, and the system experiences a decrease in entropy during the process. The exothermic effect (reflected by the absolute value of ΔH^0) and the reduction in system disorder (represented by the absolute value of ΔS^0) are more pronounced for *S. aureus* than for *E. coli*. This suggests that *S. aureus* may interact more strongly with the adsorbent, leading to greater heat release and a more significant decrease in entropy during adsorption. Furthermore, the trend observed in Fig. S7(c), which shows a decline in equilibrium adsorption capacity with increasing temperature, supports the conclusion that the adsorption process is exothermic.

Material collection efficiency and cyclic adsorption at different dilution ratios of salt-lake brine

To further investigate the material's adsorption capacity for microorganisms in brine, the adsorption efficiencies of *E. coli* and *S. aureus* were evaluated in brine solutions diluted 100-, 500-, 1000-, 2000-, and 5000-fold. As shown in Fig. S8(a), the maximum adsorption efficiency for both bacterial strains was observed at a 500-fold dilution of brine. The adsorption efficiency for *E. coli* remained relatively stable across dilutions, whereas a significant decrease in the adsorption efficiency for *S. aureus* was observed at a 100-fold dilution. This variation may be attributed to changes in the material's surface charge under high-salt conditions, which could influence bacterial adsorption behavior.

Furthermore, under a 500-fold dilution of saturated brine from Chaka Salt Lake, the cyclic adsorption performance of the Fe_3O_4@SiO_2@NH_2-FLX material was evaluated using *E. coli* and *S. aureus*. A total of five consecutive adsorption-desorption cycles were conducted for each bacterial strain. As illustrated in Fig. S8(b), the material exhibited an adsorption efficiency exceeding 95% during the initial adsorption stage. In the subsequent four cycles, the adsorption efficiency remained above 80% for both bacterial strains,

further demonstrating the material's promising potential for practical applications in microbial adsorption within salt-lake environments.

Capture of halophilic bacteria in brine by different materials

The bacterial capture test results for Fe_3O_4@SiO_2@NH_2-FLX, Fe_3O_4@SiO_2@NH_2, and Fe_3O_4@SiO_2 are shown in Fig. S9. In actual saline samples, Fe_3O_4@SiO_2@NH_2-FLX demonstrated highly efficient bacterial enrichment, achieving an 89% capture efficiency for halophilic bacteria. Fe_3O_4@SiO_2@NH_2 achieved a capture efficiency of 67%, while the capture capability of Fe_3O_4@SiO_2 was relatively weak at only 13%. These results confirm the practical application potential of Fe_3O_4@SiO_2@NH_2-FLX in reagent brine solutions.

CONCLUSION

In this study, to address the low microbial capture efficiency of magnetic nanomaterials due to poor dispersion in high-salt environments, the magnetic nanoparticles were further improved and modified to prepare Fe_3O_4@SiO_2@NH_2-FLX. Adsorption experiments have shown that under optimal conditions, adsorption of the material onto *E. coli* and *S. aureus* is a spontaneous, exothermic process that is mainly chemical and occurs via monolayer adsorption. An increase in temperature will inhibit the adsorption process. Moreover, the adsorption sites of *E. coli* are relatively uniform, while those of *S. aureus* may show some non-uniformity. Under the brine system of the Chaka Salt Lake, the adsorption efficiency at a dilution ratio of 500 times is the best, and even after five cycles, adsorption still reaches over 80%. The adsorption comparison of different materials shows that under the combined action of the bifunctional groups (NH_2 and FLX groups) of the materials, the adsorption efficiency of the materials is significantly enhanced, the surface charge of the materials is improved in more complex environments, and bacterial activity can be inhibited. FLX itself, as a broad-spectrum and long-acting quinolone antibiotic, has a good inhibitory effect on aerobic bacteria and some facultative anaerobic bacteria. Adsorption tests on halophilic bacteria using actual salt-lake samples demonstrate the continued effective adsorption performance of the material. In actual research work, it can be used to capture and screen some anaerobic bacterial species at the same time. It has certain guiding significance for the capture of non-culturable strains, unknown drug-resistant bacteria, and unknown strains in extreme environments.

Appendix A. Supplementary data

Supplementary data associated with this article can be found at https://dx.doi.org/10.2306/scienceasia1513-1874.2026.018.

Acknowledgements: This work was supported by Qinghai Province Thousand Talents Program funded project (k992058).

REFERENCES

1. Aggarwal N, Kitano S, Puah GRY, Kittelmann S, Hwang IY, Chang MW (2022) Microbiome and human health: Current understanding, engineering, and enabling technologies. *Chem Rev* **123**, 31–72.
2. Saccò M, White NE, Harrod C, Salazar G, Aguilar P, Cubillos CF, Meredith K, Baxter BK, et al (2021) Salt to conserve: A review on the ecology and preservation of hypersaline ecosystems. *Biol Rev* **96**, 2828–2850.
3. Bhardwaj S, Badiyal A, Dhiman S, Bala J, Walia A (2025) Exploring halophiles for reclamation of saline soils: Biotechnological interventions for sustainable agriculture. *J Basic Microbiol* **65**, 20.
4. Ding Y, Ke J, Hong T, Zhang A, Wu X, Jiang X, Shao S, Gong M, et al (2025) Microbial diversity and ecological roles of halophilic microorganisms in Dingbian (Shaanxi, China) saline-alkali soils and salt lakes. *BMC Microbiol* **25**, 18.
5. Oren A (2024) Novel insights into the diversity of halophilic microorganisms and their functioning in hypersaline ecosystems. *npj Biodivers* **3**, 9.
6. Bowers KJ, Mesbah NM, Wiegel J (2009) Biodiversity of poly-extremophilic bacteria: Does combining the extremes of high salt, alkaline pH and elevated temperature approach a physico-chemical boundary for life? *Saline Systems* **5**, 9.
7. Oldham C (2021) Rapid bacterial capture with modified magnetic nanoparticles for sepsis diagnosis. BSc Thesis, Brigham Young University, USA.
8. Wang J, Yu G, Fang Q, Xu Y, Zhang J, Hui A, Xuan S, Leung KCF (2025) Hollow-structured nanorobot with excellent magnetic propulsion for catalytic pollutant degradation, anti-bacterial and biofilm removal. *Adv Healthcare Mater* **14**, 14.
9. Yang Y (2014) Efficient removal of pathogenic bacteria and viruses by multifunctional amine-modified magnetic nanoparticles. MSc Thesis, Nankai University, China.
10. Hoijang S, Ananta S (2025) Surface modification of magnetic nanoparticles for selective adsorption of organic dyes: A mini-review. *ScienceAsia* **51S**, ID 2025s012.
11. Dong J (2020) Preparation of magnetic nanocomosite particles and their applications in antibacterial activity and capturing *Staphylococcus aureus*. MSc Thesis, Jilin University, China.
12. Li W, Bai X, Xiao F, Huang J, Zeng X, Xu Q, Song Y, Xu X, et al (2023) MXene@Au based electrochemical biosensor with pretreatment by magnetic nanoparticles for determination of MRSA from clinical samples. *J Hazard Mater* **457**, 131823.
13. Wen C, Zhang Y, Zeng J (2022) Comprehensive experiment of capture and separation of bacteria with superparamagnetic nanoclusters. *Exp Technol Manag* **39**, 51–56.
14. Yang X, Zhou X, Zhu M, Xing D (2017) Sensitive detection of *Listeria monocytogenes* based on highly efficient enrichment with vancomycin-conjugated brush-like magnetic nano-platforms. *Biosens Bioelectron* **91**, 238–245.

15. Rashid M, Rabbi MA, Ara T, Hossain MM, Islam MS, Elaissari A, Ahmad H, Rahman MM (2021) Vancomycin conjugated iron oxide nanoparticles for magnetic targeting and efficient capture of Gram-positive and Gram-negative bacteria. *RSC Adv* **11**, 36319–36328.
16. Abafogi AT, Lee J, Kim J, Lee SW, Jang S, Park S (2024) Automated sepsis detection with vancomycin- and allantoin-polydopamine magnetic nanoparticles. *Sci Rep* **14**, 3693.
17. Li Y, Qi Y, Liu J, Wang P, Zheng J, Chen X, Wang Y, Zhao X, et al (2025) Antibiotic-modified nanoparticles combined with lysozyme for rapid extraction of pathogenic bacteria DNA in blood. *Anal Chem* **97**, 6201–6210.
18. Upadhyay RG, Singh PK (2024) Strategies to combat drug resistance: Innovations and challenges: A review. *Biosci Biotechnol Res Asia* **21**, 537–545.
19. Wu G, Zhou J, Zhang J (2014) Study on antibacterial activity of 5 kinds of quindones *in vitro*. *Chin J Clin Pharmacol* **30**, 129–130, 159.
20. Fan G, Ren Y, Jiang W, Wang C, Xu B, Liu F (2014) Effective catalytic hydrodechlorination of 4-chlorophenol over a Rh immobilized on amine-functionalized magnetite nanoparticles in aqueous phase. *Catal Commun* **52**, 22–25.
21. Huang Y, Wang Y, Yan X (2010) Amine-functionalized magnetic nanoparticles for rapid capture and removal of bacterial pathogens. *Environ Sci Technol* **44**, 7908–7913.
22. Reddy PM, Chang K-C, Liu Z-J, Chen C-T, Ho Y-P (2014) Functionalized magnetic iron oxide (Fe_3O_4) nanoparticles for capturing Gram-positive and Gram-negative bacteria. *J Biomed Nanotechnol* **10**, 1429–1439.
23. Wang J, Zheng S, Shao Y, Liu J, Xu Z, Zhu D (2010) Amino-functionalized Fe_3O_4@SiO_2 core-shell magnetic nanomaterial as a novel adsorbent for aqueous heavy metals removal. *J Colloid Interface Sci* **349**, 293–299.
24. Yuan B, An Q, Xiao Z, Hao J, Zhu K, Zhai S, Ha C-S (2023) Polyethyleneimine-integrated composite sorbents for emerging pollutants remediation in water: Cross-linking strategy and tailored affinity. *Resour Chem Mater* **2**, 231–244.
25. Ding S, Yousef F, Wei J, Wei Wang, Xie R, Liu Z, Ju X, Chu L (2020) Antimicrobial peptide-functionalized magnetic nanoparticles for rapid capture and removal of pathogenic bacteria. *Microchem J* **159**, 105493.
26. Chen B, Xie H, Zhang A, Liu N, Li Q, Guo J, Su B (2019) Synthesis of PEI-functionalized magnetic nanoparticles for capturing bacteria. *J Wuhan Univ Technol Mater Sci Ed* **34**, 236–242.
27. Rostamizadeh S, Estiri H, Azad M (2016) Facile method for the synthesis of core/shell Fe_3O_4@SiO_2@SiO_2-SH-Au: A super magnetic nanocatalyst for water-medium and solvent-free alkyne hydration. *J Iran Chem Soc* **13**, 1367–1374.
28. Guo Q, Zhang B, Yang Z, Wang Q, Wang Q, Wen G (2025) Construction of antimicrobial CeO_2/Fe_2O_3 nanomaterials with enzyme-like activity and study of their mechanisms. *Sep Purif Technol* **353**, 128448.
29. Li C, Li Z, Gan Y, Jiang F, Zhao H, Tan J, Yang Y, Yuan P, et al (2022) Selective capture, separation, and photothermal inactivation of methicillin-resistant *Staphylococcus aureus* (MRSA) using functional magnetic nanoparticles. *ACS Appl Mater Interfaces* **14**, 20566–20575.
30. Shi Z, Zhang Y, Dai R, Chen S, Zhang M, Jin L, Wang J, Zhao W, et al (2020) Rationally designed magnetic poly(catechol-hexanediamine) particles for bacteria removal and on-demand biofilm eradication. *Colloids Surf B* **186**, 110728.
31. Darabdhara G, Boruah PK, Hussain N, Borthakur P, Sharma B, Sengupta P, Das MR (2017) Magnetic nanoparticles towards efficient adsorption of gram positive and gram negative bacteria: An investigation of adsorption parameters and interaction mechanism. *Colloids Surf A* **516**, 161–170.
32. Pham TD, Nguyen PT, Phan TMN, Dinh TD, Tran TMH, Nguyen MK, Hoang TH, Srivastav AL (2024) Highly adsorptive removal of ciprofloxacin and *E. coli* inactivation using amino acid tryptophan modified nano-gibbsite. *Environ Res* **258**, 119396.
33. Ferreira M, Sousa CF, Gameiro P (2020) Fluoroquinolone metalloantibiotics to bypass antimicrobial resistance mechanisms: Decreased permeation through porins. *Membranes* **11**, 3.
34. Vergalli J, Atzori A, Pajovic J, Dumont E, Malloci G, Masi M, Vargiu AV, Winterhalter M, et al (2020) The challenge of intracellular antibiotic accumulation, a function of fluoroquinolone influx versus bacterial efflux. *Commun Biol* **3**, 198.
35. Zhao YF, Zhang J, P ZJ (2023) Joint toxic effects of two fluoroquinolones antibiotics and quorum sensing inhibitors on *E. coli*. *Asian J Ecotoxicol* **18**, 27–38.
36. Deng S, Upadhyayula VKK, Smith GB, Mitchell MC (2008) Adsorption equilibrium and kinetics of microorganisms on single-wall carbon nanotubes. *IEEE Sens J* **8**, 954–962.
37. Ghoshroy S, Nair VK, Smith GB, Mitchell MC, Deng S, Upadhyayula VKK (2008) Adsorption kinetics of *Escherichia coli* and *Staphylococcus aureus* on single-walled carbon nanotube aggregates. *Water Sci Technol* **58**, 179–184.
38. Upadhyayula VKK, Deng S, Smith GB, Mitchell MC (2009) Adsorption of *Bacillus subtilis* on single-walled carbon nanotube aggregates, activated carbon and NanoCeram™. *Water Res* **43**, 148–156.
39. Khan SS, Srivatsan P, Vaishnavi N, Mukherjee A, Chandrasekaran N (2011) Interaction of silver nanoparticles (SNPs) with bacterial extracellular proteins (ECPs) and its adsorption isotherms and kinetics. *J Hazard Mater* **192**, 299–306.
40. Li B, Mao J, Wu J, Mao K, Jia Y, Chen F, Liu J (2024) Nano–Bio interactions: Biofilmtargeted antibacterial nanomaterials. *Small* **20**, 2306135.

Appendix A. Supplementary data

Table S1 XPS results of Fe_3O_4, Fe_3O_4@SiO_2@PEI, and Fe_3O_4@SiO_2@NH_2-FLX.

Adsorbent	The chemical composition (at.%)					
	Fe	F	O	C	N	Si
Fe_3O_4	5.49	0	24.39	70.11	0	0
Fe_3O_4@SiO_2@NH_2-FLX	0	2.76	33.22	36.81	8.31	17.91

Table S2 Langmuir and Freundlich isothermal adsorption parameters.

Type of bacteria	Langmuir isotherm			Freundlich isotherm		
	Q_m (CFU/g)	K_L (ml/CFU)	R^2	K_F [(CFU/g)·(CFU/ml)^n]	$1/n$	R^2
E. coli	8.613×10^{10}	3.169×10^{-6}	0.992	1.429×10^{9}	0.270	0.991
S. aureus	3.249×10^{10}	3.358×10^{-6}	0.993	3.744×10^{8}	0.276	0.808

Table S3 Pseudo-first-order and pseudo-second-order kinetic parameters.

Type of	C_0	$Q_{e,\exp}$	Pseudo-first order kinetics			Pseudo-second order kinetics		
bacteria	(CFU/ml)	(CFU/g)	K_1 (min^{-1})	R^2	$Q_{e,\mathrm{cal}}$ (CFU/g)	K_2 (g·min^{-1}·CFU^{-1})	R^2	$Q_{e,\mathrm{cal}}$ (CFU/g)
E. coli	5.40×10^{7}	2.156×10^{10}	2.378	0.996	2.155×10^{10}	1.375×10^{-9}	0.999	2.159×10^{10}
S. aureus	6.55×10^{7}	3.331×10^{10}	2.934	0.149	3.02×10^{10}	1.014×10^{-10}	0.999	3.365×10^{10}

Table S4 Adsorption thermodynamic parameters.

Temperature (K)	*E. coli*				*S. aureus*			
	$\ln K_T$	ΔG^0 (KJ/mol)	ΔH^0 (KJ/mol)	ΔS^0 [J/(mol·K)]	$\ln K_T$	ΔG^0 (KJ/mol)	ΔH^0 (KJ/mol)	ΔS^0 [J/(mol·K)]
298	7.64	−18.93			10.13	−25.10		
303	7.50	−18.89			8.64	−21.76		
308	6.90	−17.67	−58.166	−131.03	7.91	−20.25	−110.909	−291.49
313	6.48	−16.85			7.48	−19.46		
318	6.31	−16.68			7.22	−19.09		

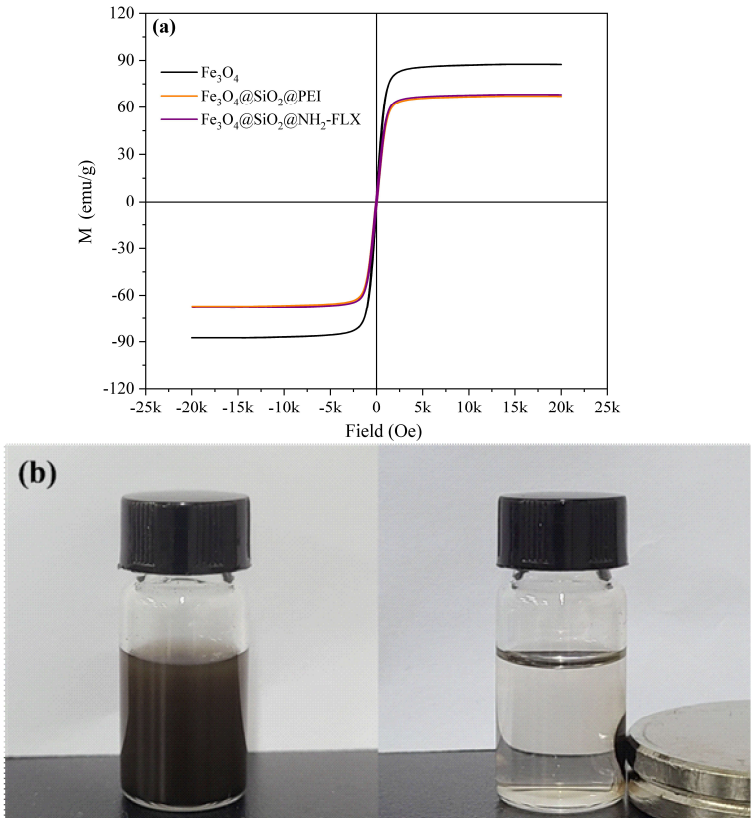

Fig. S1 (a) Hysteresis loops of Fe_3O_4@SiO_2@NH_2-FLX and Fe_3O_4 and (b) magnetic characterization photographs of Fe_3O_4@SiO_2@NH_2-FLX.

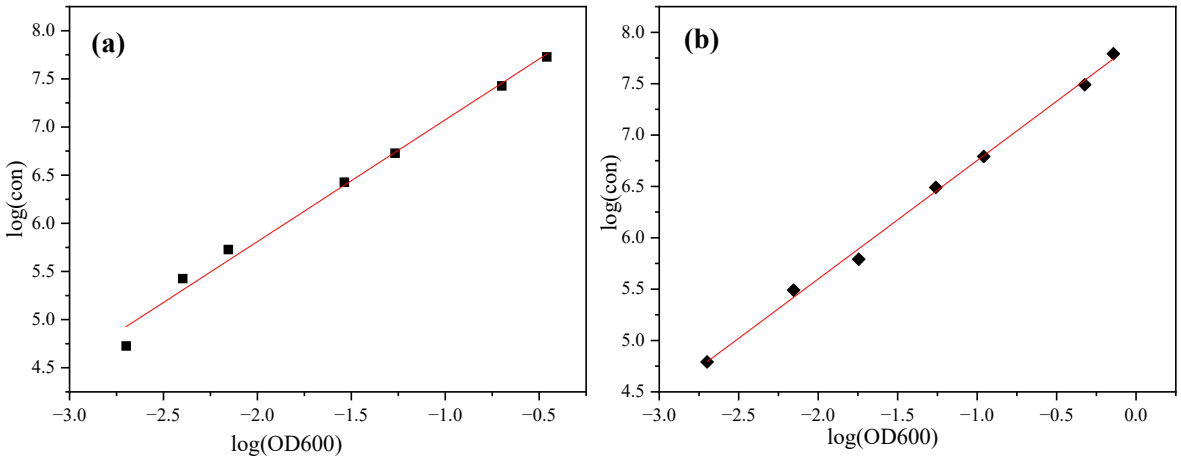

Fig. S2 Standard curves for (a) *E. coli* and (b) *S. aureus*.

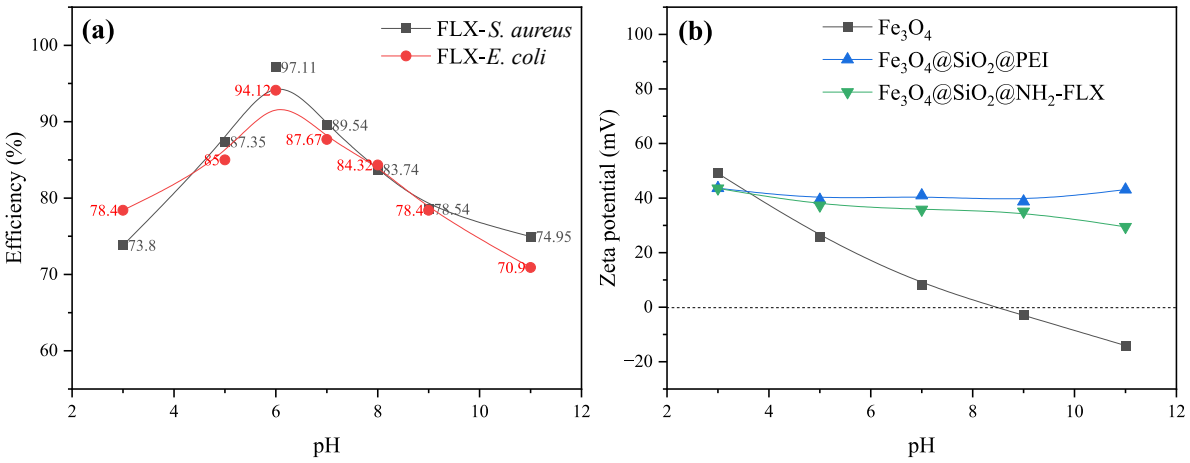

Fig. S3 (a) The effect of different pH levels on the adsorption of bacteria by materials and (b) the effect of pH on surface charge of materials.

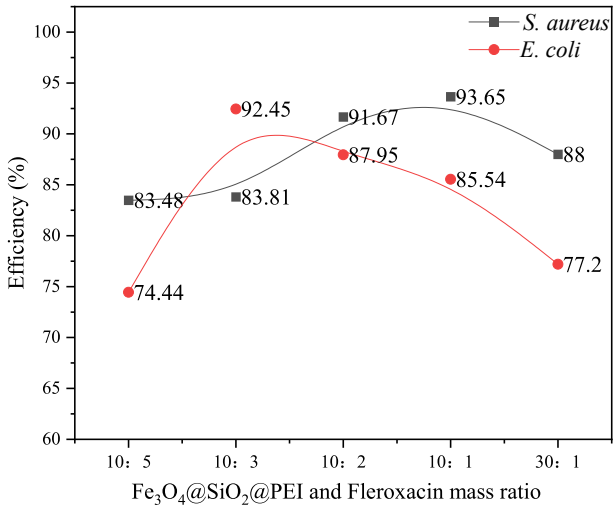

Fig. S4 The effect of different amounts of fleroxacin added on the adsorption efficiency of Fe_3O_4@SiO_2@NH_2-FLX toward *E. coli* and *S. aureus*.

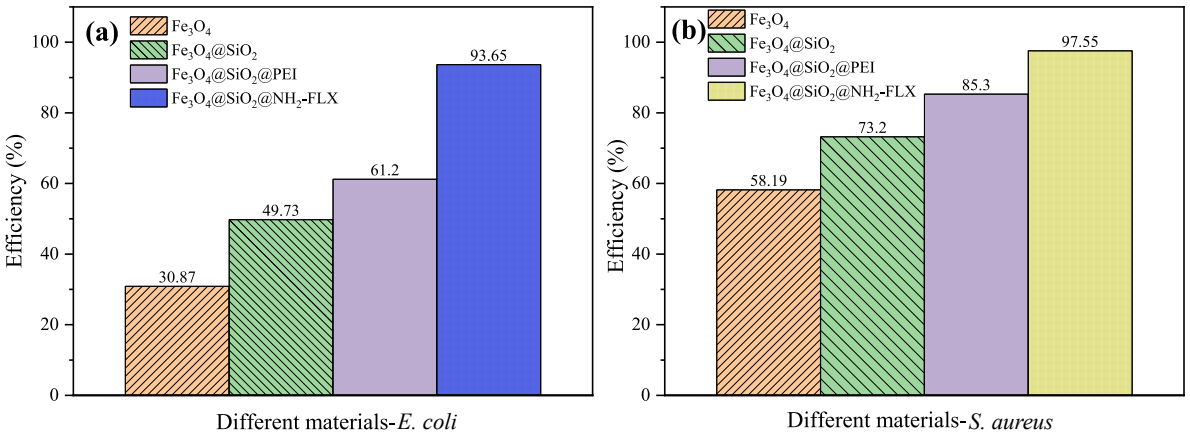

Fig. S5 Adsorption efficiency of different materials for (a) *E. coli* and (b) *S. aureus*.

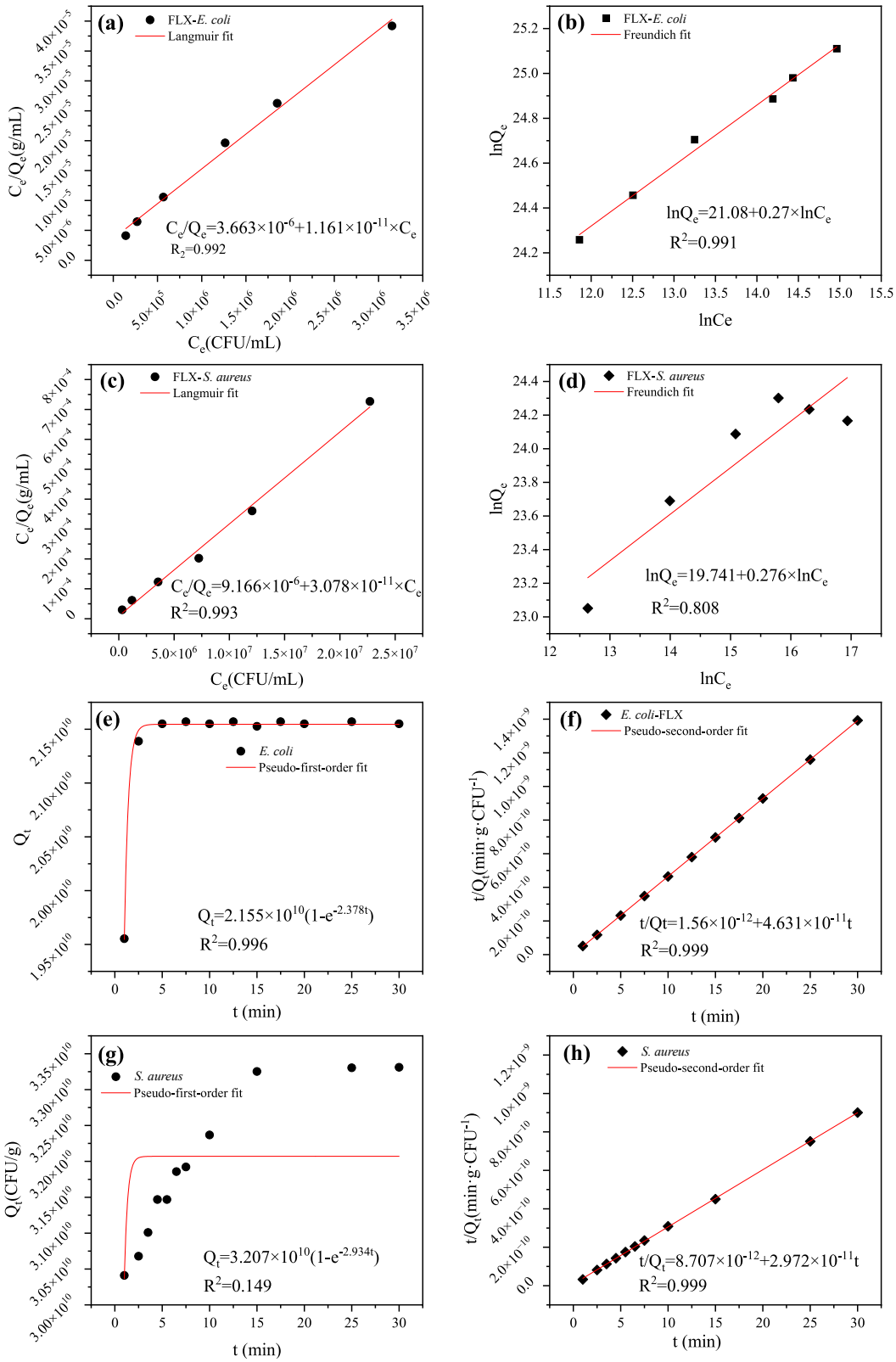

Fig. S6 (a, c) Langmuir isothermal adsorption isotherms and (b, d) Freundlich isothermal adsorption isotherms; (e, g) pseudo-first-order kinetic fitting curves and (f, d) pseudo-second-order kinetic fitting curves.

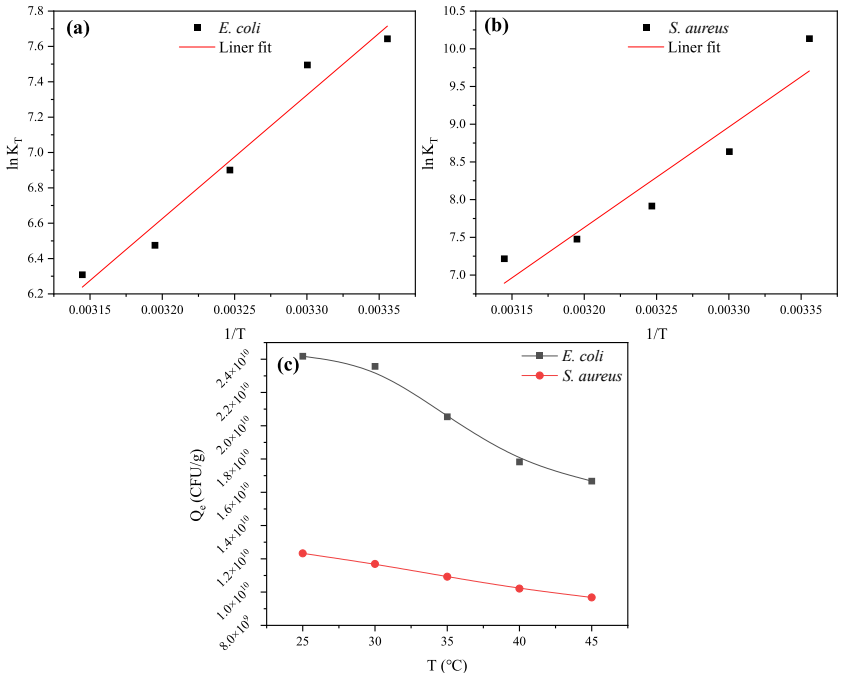

Fig. S7 (a) and (b) van't Hoff curves for the adsorption of *E. coli* and *S. aureus*, respectively, and (c) effect of temperature on bacterial adsorption by Fe_3O_4@SiO_2@NH_2-FLX.

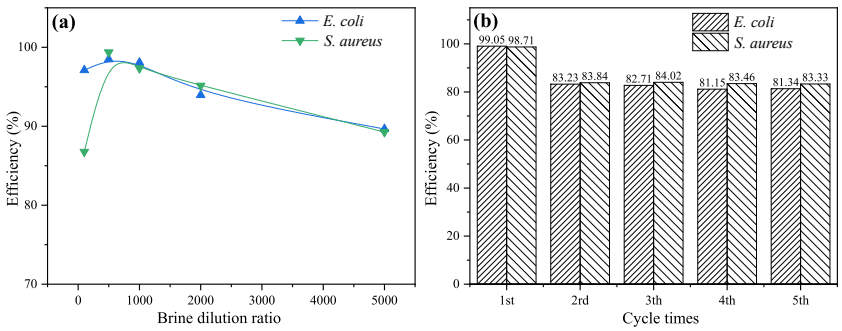

Fig. S8 (a) Bacterial adsorption efficiency of materials under different brine dilution ratios and (b) adsorption efficiency of Fe_3O_4@SiO_2@NH_2-FLX for *E. coli* and *S. aureus* after five cycles of adsorption and desorption.

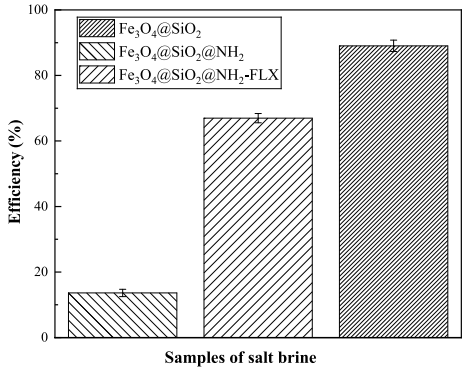

Fig. S9 The histogram of bacterial adsorption efficiency in different materials for salt lake brine ($n = 3$).